Local Structure of the Convective Boundary Layer from a Volume-Imaging Radar

BRIAN D. POLLARD*

Department of Electrical and Computer Engineering, University of Massachusetts, Amherst, Amherst, Massachusetts

SAMIR KHANNA+

Department of Meteorology, The Pennsylvania State University, University Park, Pennsylvania

STEPHEN J. FRASIER

Department of Electrical and Computer Engineering, University of Massachusetts, Amherst, Amherst, Massachusetts

JOHN C. WYNGAARD AND DENNIS W. THOMSON

Department of Meteorology, The Pennsylvania State University, University Park, Pennsylvania

ROBERT E. MCINTOSH

Department of Electrical and Computer Engineering, University of Massachusetts, Amherst, Amherst, Massachusetts

(Manuscript received 7 December 1998, in final form 31 August 1999)

ABSTRACT

The local structure and evolution of the convective boundary layer (CBL) are studied through measurements obtained with a volume-imaging radar, the turbulent eddy profiler (TEP). TEP has the unique ability to image the temporal and spatial evolution of both the velocity field and the local refractive index structure-function parameter, $\tilde{C}_n^2$. Volumetric images consisting of several thousand pixels are typically formed in as little as 1 s. Spatial resolutions are approximately 30 m by 30 m by 30 m.

CBL data obtained during an August 1996 deployment at Rocks Springs, Pennsylvania, are presented. Measurements of the vertical $\tilde{C}_n^2$ profile are shown, exhibiting the well-known bright band near the capping inversion at z_i, as well as intermittent plumes of high $\tilde{C}_n^2$. Horizontal profiles show coherent 100-m-scale $\tilde{C}_n^2$ and vertical velocity (w) structures that correspond to converging horizontal velocity vectors. To quantify the scales of structures, the vertical and streamwise horizontal correlation distances are calculated within the TEP field of view.

To study the statistics and scales of larger structures, effective volumes larger than the TEP field of view are constructed through Taylor's hypothesis. Statistics of $\tilde{C}_n^2$ and w time series are compared to an appropriately scaled large eddy simulation (LES). While w time series comparisons agree very well, the LES $\tilde{C}_n^2$ predictions agree only with some of the measured data. Finally, the scales of $\tilde{C}_n^2$ structures in the TEP time series measurements are calculated and compared to the scales in the LES spatial domain. Good agreement is found only near the capping inversion layer, the area of largest structures. This study highlights the unique capabilities of the TEP instrument, and shows what are believed to be the first statistical comparisons of measured $\tilde{C}_n^2$ data with LES derived results.

1. Introduction

The behavior of refractive index gradients in the atmospheric boundary layer (ABL) has long been of interest in electromagnetic propagation studies. Sensitive radars in the VHF, UHF, and lower microwave frequency ranges can measure the backscattered power from refractive index variations in the clear atmosphere, and since the mid-1960s researchers have used such radars to study the morphology of those variations in the convective boundary layer (CBL). Much of that early work is reviewed in Gossard (1990).

The radars used in CBL morphology studies are usually of two types: mechanically scanned systems and vertically pointed, nonscanning systems. The scanning systems are typically employed in the study of kilometer-scale or larger features (Hardy and Ottersten

* Current affiliation: Jet Propulsion Laboratory, California Institute of Technology, Pasadena, California.

+ Current affiliation: Telecommunications Products Division, Corning Inc., Corning, New York.

Corresponding author address: Stephen J. Frasier, Knowles Engineering Building, University of Massachusetts, Amherst, MA 01003. E-mail: frasier@ecs.umass.edu

1969; Konrad 1970; Doviak and Berger 1980). Such features typically remain coherent for as long as 60 min (Doviak and Berger 1980), and thus the one to several minute scan time of those systems is not an issue. Vertically or near vertically pointed systems are either very high resolution FM–CW systems (Richter 1969; Gossard et al. 1982; Eaton et al. 1995), or UHF or microwave profilers (Ecklund et al. 1988; White et al. 1991; Ecklund et al. 1999). Those systems provide information about CBL vertical structure with spatial resolutions from 1 to 100 m. The temporal resolutions are typically 30 s to as fine as 1 s, and give useful insights into the temporal evolution of local features in the vertical profile.

The Turbulent Eddy Profiler (TEP) radar system recently reported in Mead et al. (1998) provides the spatial and temporal resolution of current vertically pointed profiler systems, while adding horizontal spatial coverage through the use of digital beam-forming techniques. TEP forms three-dimensional images consisting of several thousand volumetric pixels of the backscattered power and Doppler velocity within a 25° cone above the radar. The pixel resolution is on the order of 30 m × 30 m × 30 m, and the image formation time is on the order of 1 s. Those features give TEP the unique ability to study the three-dimensional behavior of refractive index structures and velocity vectors in the ABL with a high-temporal resolution.

In August 1996 TEP was deployed at Rock Springs, Pennsylvania, near The Pennsylvania State University (PSU). Also present at the measurement site was an array of sonic anemometers that measured the surface temperature flux, convective velocity scale, and other parameters. In this paper we present radar observations from a highly convective boundary layer encountered during that deployment. The qualitative, three-dimensional structure and evolution of the local reflectivity ($\tilde{\eta}$) and vertical velocity (w) fields measured by TEP are shown. We then calculate the appropriate correlation distances from the three-dimensional autocorrelation function, quantifying the scales of local structures in a manner similar to previous studies (Deardorff and Willis 1985; Lenschow and Stankov 1986; Mason 1989). The statistical variabilities of $\tilde{\eta}$ and w measurements are also examined through the analysis of TEP time series data.

We compare many of the presented TEP measurements to CBL predictions of a large eddy simulation (LES). LES has often been applied to studies of the three-dimensional structure of CBL velocity fields (Moeng 1984; Mason 1989; Schmidt and Schumann 1989; Khanna and Brasseur 1998), and recent work (Peltier and Wyngaard 1995; Khanna and Wyngaard 1997) suggests that LES can also be applied to studies of refractive index structures through the calculation of the local refractive index structure–function parameter, $\tilde{C}_n^2$. TEP is an appropriate system for LES comparisons due to both its pixel size, which is similar to the 60 m × 60 m × 16 m pixel of LES (Khanna and Brasseur 1998), and its volume-imaging ability that can be compared with the three-dimensional, time-varying fields predicted by LES.

The following section of this paper describes the TEP system and briefly discusses the analysis techniques employed on the acquired data. Section 3 reviews the experimental setup and discusses the meteorological and in situ parameters from the TEP dataset. Section 4 presents qualitative and quantitative measurements from the TEP CBL dataset. Section 5 reviews our method of calculating $\tilde{C}_n^2$ from LES and presents qualitative LES results. Statistical comparisons of TEP time series measurements and LES appear in section 6 and concluding remarks are found in section 7.

2. Radar measurements

TEP (Mead et al. 1998) is a 915-MHz volume-imaging radar system that uses digital beam-forming techniques to obtain high-resolution measurements in the ABL. The vertical (range) resolution is 30 m and the horizontal (azimuthal) resolution is 4.5°. At a height of 380 m, a pixel has a horizontal extent of 30 m. Figure 1 shows TEP deployed at the Rock Springs site near the PSU campus at University Park, Pennsylvania.

In normal operation a vertically pointed horn antenna illuminates a 25° conical volume of the ABL above a 60 element receiver array. Each element of the array receives the backscattered signal from the full field of view. Echoes from each of the 50 range bins are digitized, coherently averaged, and output at a rate of 100 Hz. This dictates the range of resolvable Doppler velocities of ± 8.2 m s^{-1}. The receiver array is focused in postprocessing by combining the outputs of every receiver with appropriate phase delays. A focused beamwidth of 4.5° is obtained by processing the outputs of 60 receivers. After focusing, backscattered power and mean velocity are estimated from the first two moments of the Doppler spectrum. Figure 2 shows typical TEP power and Doppler data products for altitudes between 900 and 1200 m, averaged over a 5-s interval. The area of high intensity in the backscattered power corresponds to a coherent, downward velocity feature.

TEP estimates the velocity vector and local volume backscattered power coefficient, which we label as $\tilde{\eta}$, in each of its pixels and the estimation techniques are discussed in Mead et al. (1998). To calculate $\tilde{\eta}$, an absolute calibration of the system is necessary. For this deployment, TEP is calibrated using a cross-dipole target on a tethered balloon flown above the receiver array.

To obtain C_n^2 from the backscattered power, the relationship of Ottersten (1969) is often used

$$\eta \approx 0.38 C_n^2 \lambda^{-1/3}, \tag{1}$$

where λ is the radar wavelength. The C_n^2 of (1) is the traditional structure–function parameter defined through an ensemble average (Tatarskii 1971):

$$\langle [n(\mathbf{x}, t) - n(\mathbf{x} + \mathbf{r}, t)]^2 \rangle = C_n^2 r^{2/3}, \tag{2}$$

FIG. 1. A photo of the TEP system in Rock Springs, PA. The foreground of the photo shows the receiver array encased within a clutter fence. Visible behind the array is the transmitter horn and the operations trailer.

for inertial subrange separations $r = |\mathbf{r}|$, where $n(\mathbf{x}, t)$ is the index of refraction at a point $\mathbf{x}$ and time t, and the brackets, $\langle \cdot \rangle$, denote an ensemble average.

The roots of (1) and (2) lie in the hypotheses of Kolmogorov (1941) concerning the structure of turbulence in the inertial subrange. Also central to (1) and (2) is the notion of the ensemble average. These equations are purely statistical relations that emerge only after averaging over a sufficiently large number of realizations of the flow. In practice, to obtain η and C_n^2, we average over time, invoking the ergodic hypothesis (Tennekes and Lumley 1972) that in a statistically steady flow a time average converges to the ensemble average.

For many radar measurements, (1) can be used to a good approximation in obtaining C_n^2 from measured values of η. Equation (1) is not a good approximation, however, for systems such as TEP with 10-m-scale pixels and short averaging times. In such systems, the η values fluctuate considerably in time and space; the expected values of η and squared two-point difference in the refractive index, however, vary only on the timescale of the mean-flow evolution, and on the spatial scale of the mean-flow structure. The faster, smaller-scale variations in backscattered power and in refractive-index structure are often erroneously interpreted as variations in η and in C_n^2.

To clarify this issue, Peltier and Wyngaard (1995) introduced local variables, similar to the volume-averaged, finescale properties discussed in Kolmogorov (1962) and Obukhov (1962). The local refractive-index structure–function parameter $\tilde{C}_n^2$ of Peltier and Wyngaard is a random quantity averaged over a volume of scale r. Its expected value is the traditional C_n^2 of (2):

$$\langle \tilde{C}_n^2 \rangle = C_n^2. \tag{3}$$

The local, volume-averaged backscattered power as measured by TEP is then denoted $\tilde{\eta}$, and the analogous equation to (1) is

$$\tilde{\eta} \approx 0.38 \tilde{C}_n^2 \lambda^{-1/3}. \tag{4}$$

As we discuss in appendix A, we do not, in general, expect $\tilde{\eta}$ to correlate perfectly with $\tilde{C}_n^2$ on a point by point basis. However, for the measurements that follow we assume that $\tilde{\eta}$ and $\tilde{C}_n^2$ are perfectly correlated, and examine that assumption in appendix A.

A separate issue regarding (4) is the assumption that the dominant scattering mechanism is Bragg scattering, or scattering from spatial fluctuations in the index of refraction at a characteristic scale of $\lambda/2$. One consideration in estimating $\tilde{\eta}$ is the effect of non-refractive-index scatterers in the TEP volume. Recent results (Wilson et al. 1994; Ecklund et al. 1996) suggest that biological targets such as birds and insects can contribute substantially to the backscattered power at 915 MHz. Both Wilson et al. (1994) and Ecklund et al. (1996) find that in a typical CBL over land, insects tend to be the dominant scattering mechanism in the lower half of the CBL. To mitigate that problem, we follow the approach of (Angevine et al. 1994), and statistically filter the data in each pixel, discarding data values that fall outside of

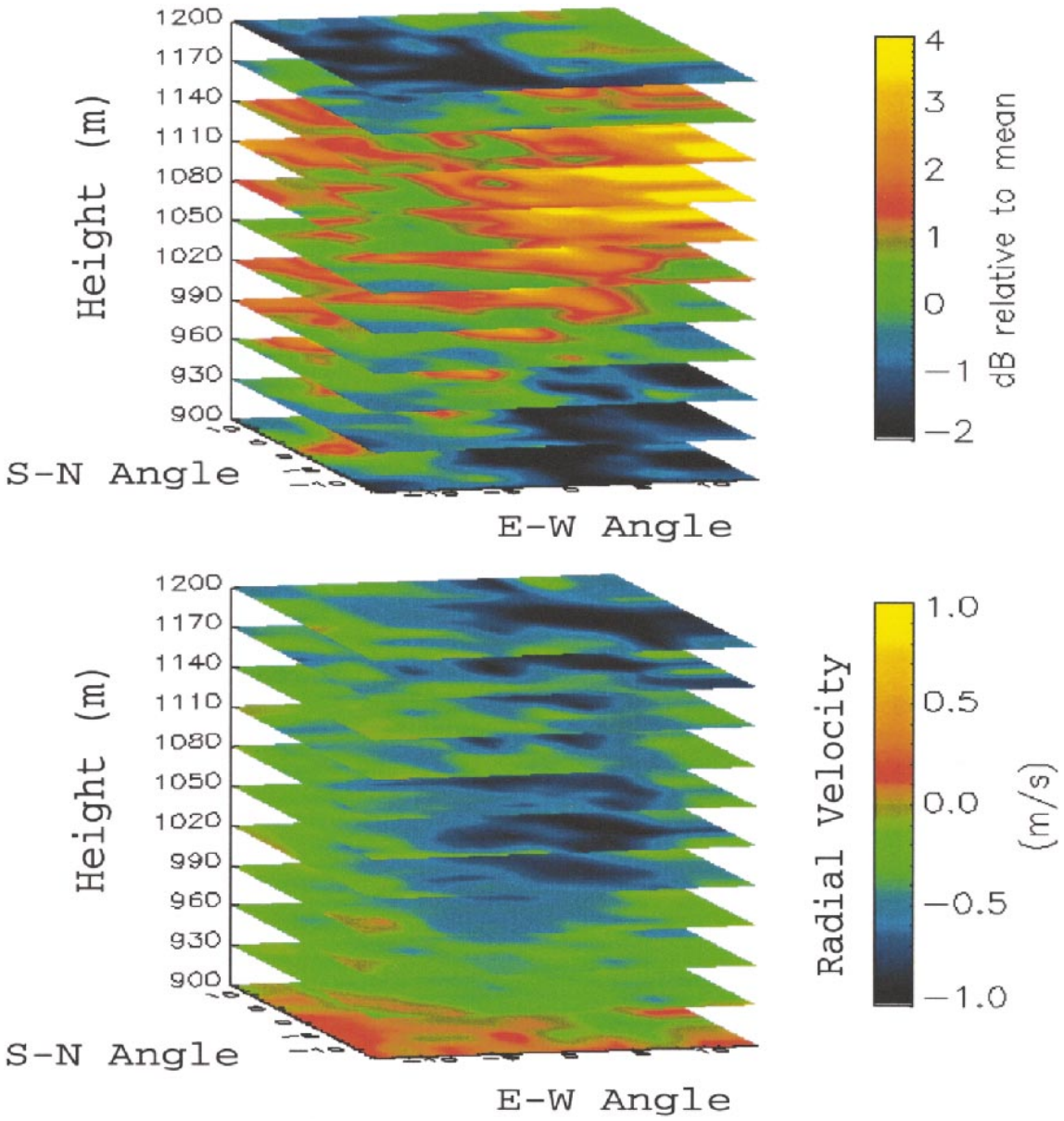

FIG. 2. Snapshots of backscattered intensity and radial velocity from the TEP system. The horizontal axes represent the angle off of zenith, and the averaging time of the images is 5 s. The area of high-relative intensity is seen to correspond to a coherent downdraft feature in radial velocity.

three standard deviations from the local 30-s running intensity mean. Similarly, velocity measurements that fall outside of five standard deviations are discarded.

3. Description of the experiment

Figure 3 illustrates the August 1996 site plan of the Rock Springs, Pennsylvania, site. TEP is situated between two fields, approximately 30 m from a road. A horizontal array of anemometers is located approximately 300 m from TEP. In addition, a nearby operations building contains a variety of meteorological sensors for collecting ground level winds, humidity, temperature, and other parameters.

The ground station parameters for the afternoon data are shown in Table 1. Ground level winds are in the range of 1–2 m s^{-1} from the west, or near the direction of acceptable winds as illustrated in Fig. 3. The temperature rises from 1200 eastern daylight savings time EDT) values near 24° to over 26°C in the late afternoon and there is little or no cloud cover.

The naming convention for the data segments presented in this paper is outlined in Table 2. The 40–50-s gaps occurring between 10-min data segments are due

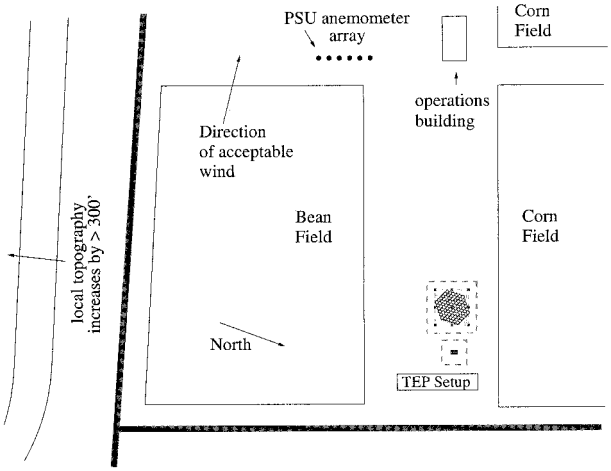

FIG. 3. The layout of the experiment site at Rock Springs, PA, six miles from the PSU campus. TEP and the anemometer array are separated by a distance of approximately 300 m. The local clutter environment includes fields of beans and corn and the area is flat except for a ridge to the south where the local topography increases by more than 300 ft.

to the data storage scheme used. For brevity, the segments are referred to by the letter of their label (i.e., N, O, P) throughout this paper.

The anemometer array was operated on 22 August beginning at 13 09 EDT for approximately 1 h. It measured the surface temperature flux $\langle w\theta \rangle_s$ and the friction velocity u_*, from which the Monin–Obukhov length scale L is calculated (Tennekes and Lumley 1972, p. 100). The measured geostrophic wind is taken from the TEP dataset as the average mean wind above z_i, and the measured mean boundary layer depth z_i is found from the maximum power return as suggested by (Wyngaard and LeMone 1980) and as implemented in (Angevine et al. 1994), among others. The measurement of z_i allows the calculation of the convective velocity scale w_* (Stull 1988, p. 118). The moisture flux was not measured. Table 3 summarizes the results obtained with the anemometer array.

The LES results provided for comparisons are also summarized in Table 3. The simulations were generated using the code of (Moeng 1984), with a 128 × 128 × 128 grid in a 5 km × 5 km × 2 km domain, and originally appeared in Khanna and Brasseur (1998). These

TABLE 1. Ground parameters measured on the afternoon of 22 August 1996.

Hour (EDT)	Wind direction (°)	Wind speed (m s^{-1})	Temp. (°C)	Relative humidity (%)
1200	241	2.4	24.1	73.4
1300	236	2.1	24.9	66.5
1400	260	1.7	25.6	59.9
1500	292	1.7	26.2	57.7
1600	270	1.8	26.4	54.6
1700	298	1.1	26.4	53.0

TABLE 2. TEP datasets collected on 22 August 1996.

Dataset name	Local start time	Local end time
	EDT	EDT
960822M	1352:32	1402:50
960822N	1403:41	1414:00
960822O	1414:53	1425:12
960822P	1425:57	1437:17
960822Q	1437:03	1447:24
960822R	1448:10	1458:29
960822S	1459:17	1509:37
960822T	1510:19	1520:38
960822U	1521:28	1531:47
960822V	1532:39	1542:58

results are not specifically matched to the conditions of 22 August 1996. In particular, the temperature jump at the top of the mixed layer on that day is not known, making it difficult to perform an LES with an exact match of the conditions. The LES set used, however, is typical of a CBL state, and the differences in features and statistics are scaled by the traditional mixed-layer scales of Deardorff (1972), z_i and w_*.

4. Morphological observations

a. Qualitative observations

A single frame of the basic TEP data products is shown in Fig. 2; we extract temporal information from a sequence of such images. Figure 4 shows plots of the backscattered power in a single, vertically pointed beam with respect to time, similar to the output of a boundary layer wind profiler. The data in the top panel of Fig. 4 is from segments M to Q, and the data in the lower panel is from segments R to V. The segments are separated by black bars that represent the downtime between data segments.

An obvious feature of the plots in Fig. 4 is the expected bright band of high $\tilde{C}_n^2$ near the capping inversion layer (Wyngaard and LeMone 1980). The top panel also shows a good deal of structure in the lower boundary layer throughout the middle three segments. In both plots, the capping inversion layer shows a modulation of ±100 m, especially in the last segment of the lower panel, V. The previous segment, U, contains a plumelike structure that creates a canopy effect in the layer surrounding z_i. Segment V follows with a collapse of z_i

TABLE 3. LES parameters and TEP measured meteorological conditions for 22 August 1996.

Parameter	LES	TEP
geostrophic wind U_g (m s^{-1})	1.0	0.9
surface temperature flux $\langle w\theta \rangle_s$ (K m s^{-1})	0.24	0.047
surface moisture flux [m s^{-1} g of vapor (kg of air)$^{-1}$]	0.05	
mean boundary layer depth z_i (m)	810	1140
Monin–Obukhov length scale L (m)	−1.6	−25
velocity scale w_* (m s^{-1})	1.85	1.20

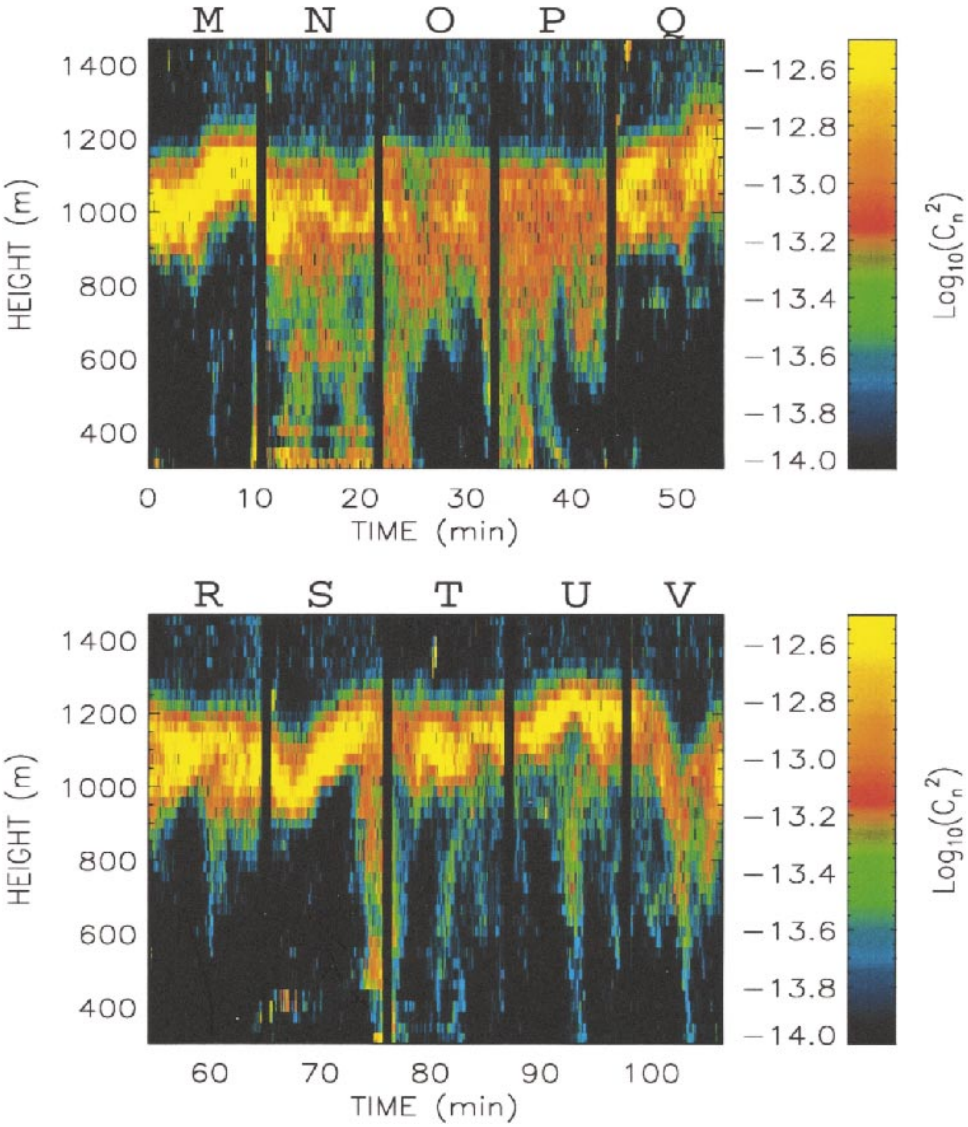

FIG. 4. Time–height plots of the TEP measured backscattered power, or $\tilde{C}_n^2$, in a single, vertically pointed beam from (top), datasets M through Q and (bottom) datasets R through V. The black bars represent missing data.

due to a deep entrainment process. The downdraft in Fig. 2 is obtained from segment V near time $t = 100$ min.

The spatial and temporal evolution of structures is observable in time sequences of horizontal slices through the field of view. Figure 5 shows a series of images of $\tilde{C}_n^2$ at a constant height of 930 m, or $z = 0.82z_i$, beginning at 1538:11 EDT. A region of high reflectivity propagates through the image from left to right with the mean wind. Each frame represents a 1.28-s average, and the time difference between frames is 5.12 s. Horizontal velocity vector estimates are overlaid on each image and converge on the area of high reflectivity. Frames of the vertical velocity, *w*, are shown in Fig. 6 corresponding to the backscatter in the Fig. 5 frames with the same horizontal velocity vectors overlaid. From these it is evident that the regions of high $\tilde{C}_n^2$ in Fig. 5 correspond to the downdraft features in *w* seen in Fig. 6.

This small downdraft feature, with a vertical extent (not shown) on the order of 60 m ($0.05z_i$), remains coherent as it advects through the TEP field of view, a time interval in excess of 40 s. It moves along the direction of the mean wind at a speed of approximately 6 m s^{-1}, over twice the measured mean wind speed at that altitude.

b. Scales of $\tilde{C}_n^2$ structures

The scales of *w* structures in the CBL are well studied. Several authors (Deardorff and Willis 1985; Lenschow and Stankov 1986; Mason 1989) use the correlation dis-

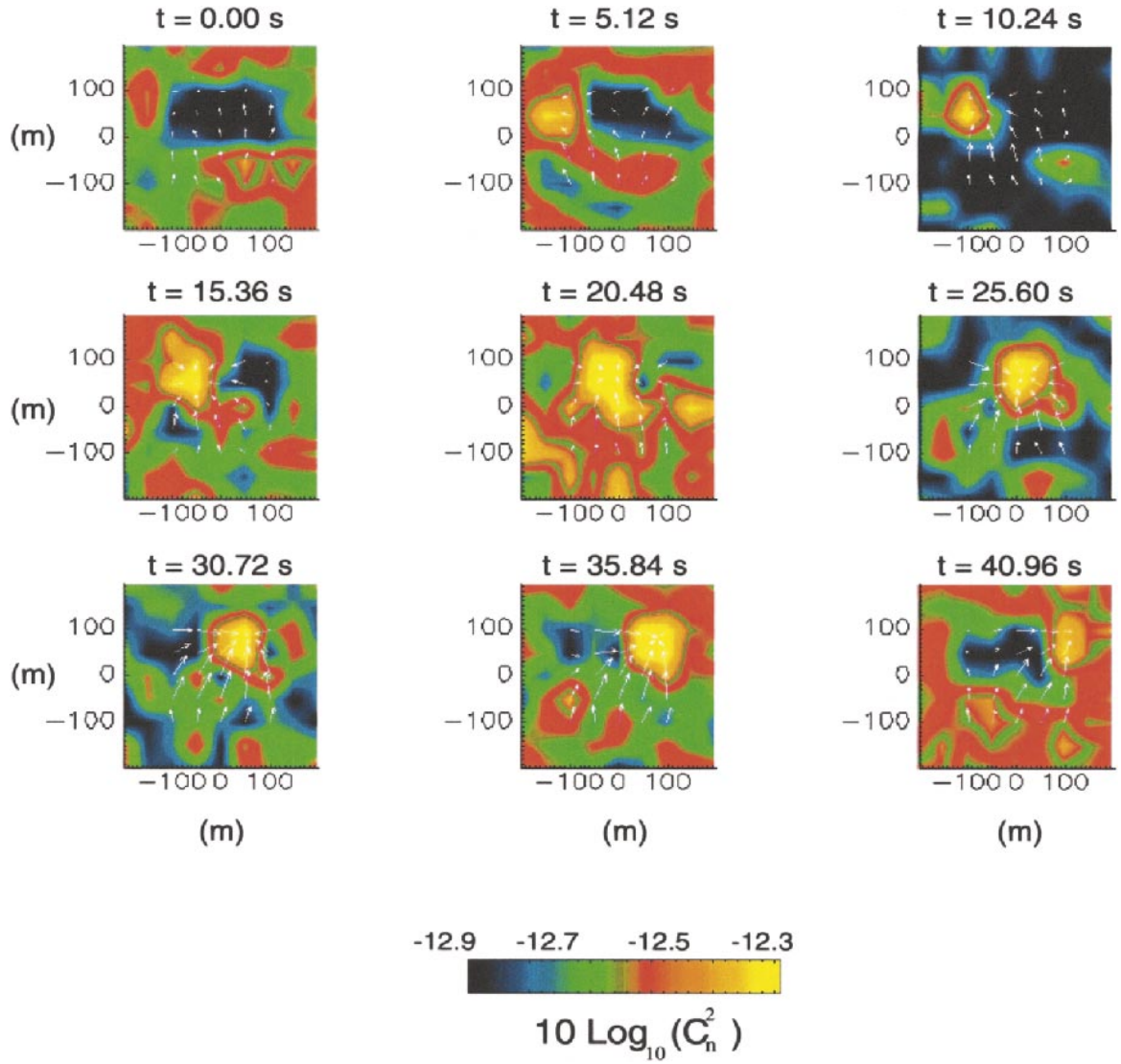

FIG. 5. A sequence of TEP $\tilde{C}_n^2$ images from an altitude of $z = 0.82z_i$ with horizontal velocity vectors overlaid. Each image is a 1.28-s average of data and the temporal spacing between images is 5.12 s.

tance λ_w from the w horizontal autocorrelation function, R_{ww}, given by

$$R_{ww} = \langle w(x)w(x + r)\rangle, \tag{5}$$

for $w(x)$ at a point x, where r is a horizontal separation distance. The correlation distance, λ_w is the point at which R_{ww} falls below e^{-1} times its peak value. In Deardorff and Willis (1985) and Mason (1989), λ_w is seen to grow with height to near the mid-boundary layer, remain constant into the upper boundary layer, and decrease as it approaches z_i.

In a similar manner, we can quantify the scales of $\tilde{C}_n^2$ structures throughout the boundary layer with TEP. Within each measurement cone, we can calculate the three-dimensional autocorrelation function for the fluctuating, zero mean component of $\tilde{C}_n^2$. This section presents measurements of λ_η, the correlation distance for the fluctuating $\tilde{C}_n^2$ autocorrelation function, $R_{\eta\eta}$, in both vertical and horizontal dimensions.

We define $R_{\eta\eta}$ as

$$R_{\eta\eta} = \langle \tilde{\eta}'(x)\tilde{\eta}'(x + r)\rangle, \tag{6}$$

where $\tilde{\eta}'(x)$ is the fluctuating component of the local volume backscattered power coefficient from a pixel at position x, and $\tilde{\eta}'(x + r)$ is the fluctuating local volume backscattered power coefficient from a pixel removed by a distance r. Here $\tilde{\eta}'$ is computed by removing the mean value at each altitude. To improve computational efficiency, $R_{\eta\eta}$ is computed from the inverse Fourier transform of the three-dimensional power spectral density of $\tilde{\eta}'$.

Each $\tilde{\eta}$ measurement is a 1.28-s average of received

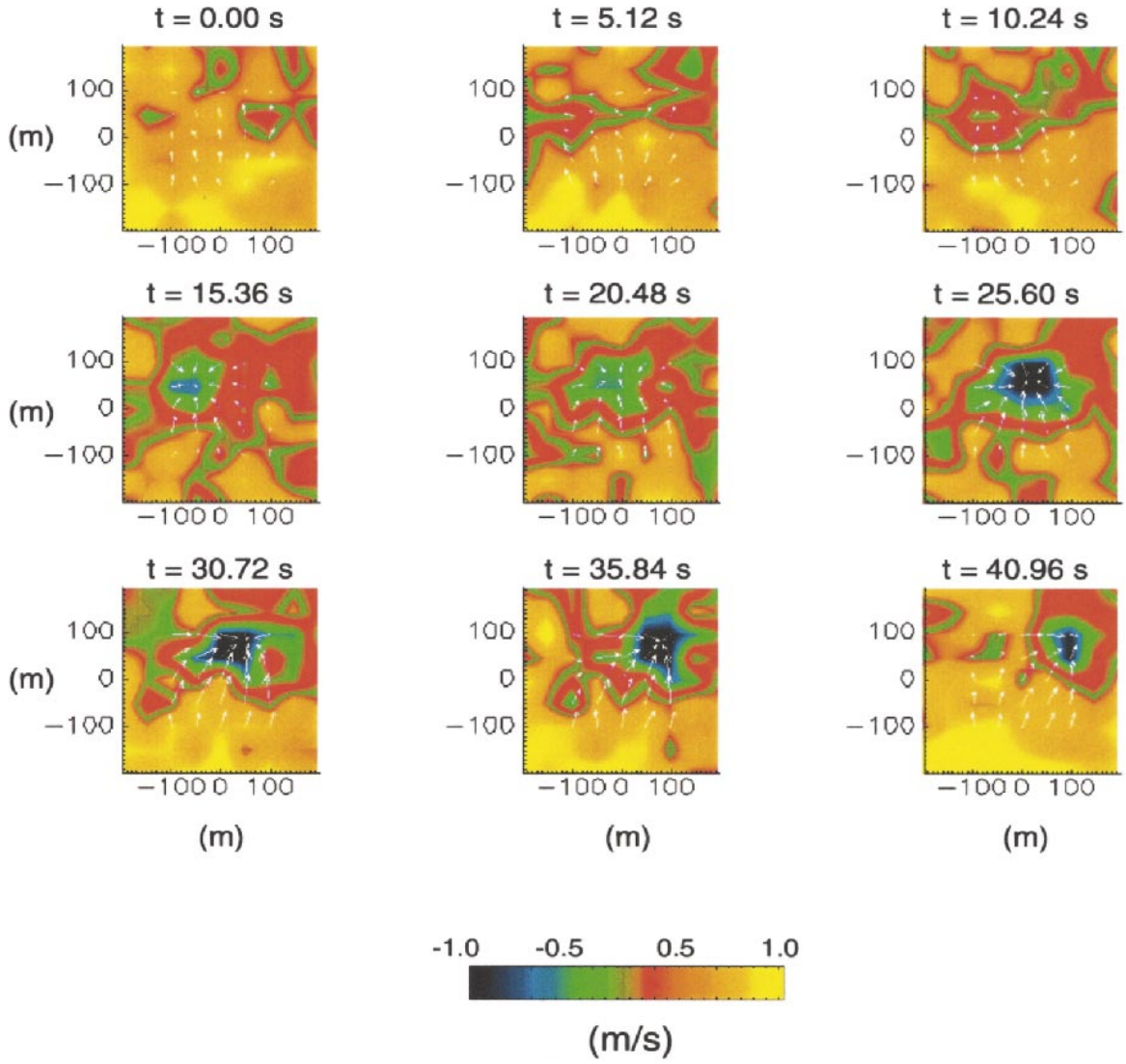

FIG. 6. A sequence of TEP vertical velocity (w) images from an altitude of $z = 0.82z_i$ with horizontal velocity vectors overlaid. These w images correspond to the $\tilde{C}_n^2$ sequence in Fig. 5, and show that the area of high intensity and converging winds in that figure corresponds to a downdraft feature in w. As in Fig. 5, the averaging time here is 1.28 s.

echoes. The $R_{\eta\eta}$ is calculated every 300 s in order to ensure each calculation is independent; in a time of 300 s, a structure moving at the mean wind speed of approximately 2 m s^{-1} should move completely through the TEP 25° field of view.

The averaged measured vertical correlation distance, $\lambda_{\eta v}$, is small, near $0.04z_i$ (45 m), on the same order as the structures in the previous section. Within each TEP cone, we examine the height dependence of $\lambda_{\eta v}$ by correlating 300-m sections of the vertical profile. The $\lambda_{\eta v}$ calculated from each of those sections remains roughly constant at approximately $0.04z_i$.

For horizontal autocorrelations, Fig. 7 shows $\lambda_{\eta h}$ along the mean wind direction calculated from all of the TEP segments listed in Table 2. Three curves are shown. The straight, dashed line represents the limits imposed by the finite field of view, and represents $\lambda_{\eta h}$ for a perfectly correlated (uniform) scene. The dashed and dotted line is $\lambda_{\eta h}$ obtained from the direct calculation of $R_{\eta\eta}$; near the upper altitudes, it is quite close to the perfectly correlated scene, suggesting that the field of view is nearly filled with large-scale structures. The solid line is $\lambda_{\eta h}$ calculated after subtracting the mean received power in each time sample at each altitude. This subtraction is a high-pass filter, removing structures in $\tilde{\eta}'$ with dimensions larger than the field of view. The high-pass $\lambda_{\eta h}$ shows several interesting characteristics. First, it agrees well with the direct $\lambda_{\eta h}$ calculation below $0.5z_i$, suggesting that TEP is capturing the full spectrum of $\tilde{C}_n^2$ features at those altitudes. Second, at $0.5z_i$ where the direct and high-pass curves diverge, the slope of the two curves differs as well. The

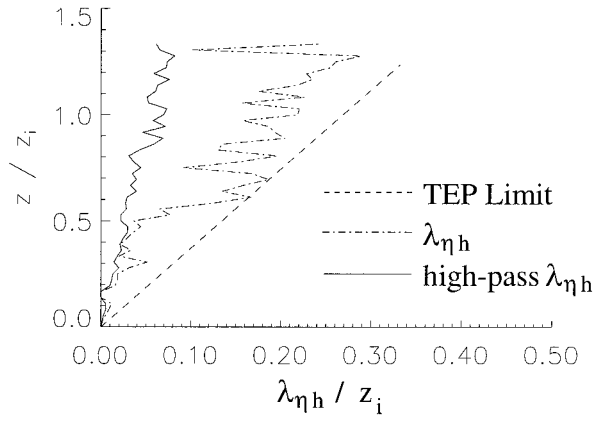

FIG. 7. The correlation length, $\lambda_{\eta h}$, for the average spatial autocorrelation function for the fluctuating component of $\tilde{C}_n^2$ within the TEP field of view. The curve labeled as the TEP limit represents a perfectly correlated scene, or the limits of the TEP measurement volume. The total $\lambda_{\eta h}$ is calculated directly from the measured $\tilde{C}_n^2$, while the high-pass $\lambda_{\eta h}$ is calculated after removing the mean value at each altitude in each measurement cone.

total curve changes to a slope similar to the perfectly correlated scene, while the high-pass curve keeps a roughly constant slope throughout the vertical profile.

Here $\lambda_{\eta h}$ quantifies the $\tilde{C}_n^2$ behavior seen in the vertical profiles in Fig. 4. Features of $\tilde{C}_n^2$ in those figures are highly intermittent in the lower boundary layer and grow slowly with height. That behavior is seen in the $\lambda_{\eta h}$ data of Fig. 7 below $0.5z_i$. Above $0.5z_i$, Fig. 4 suggests that the $\tilde{C}_n^2$ structures become quite large as they approach z_i, where they reach a maximum. Near z_i we would not expect the radar field of view to contain completely the large $\tilde{C}_n^2$ features, and that behavior is seen in Fig. 7 as $\lambda_{\eta h}$ approaches the TEP limit in the regions near z_i.

5. LES CBL features

a. LES $\tilde{C}_n^2$ calculation

The LES results included in this paper originally appeared in Khanna and Brasseur (1998). New for this paper, however, are the LES $\tilde{C}_n^2$ values. The method by which they were obtained is summarized in this section.

We calculate the refractive-index fluctuation n from the expressions presented by Wesely (1976). These expressions have the general form:

$$n = a\theta + bq, \tag{7}$$

where θ and q are the temperature and water vapor mixing ratio fluctuations, respectively, and the coefficients a and b depend on the mean values of temperature, pressure, and water vapor mixing ratio. For radio waves the effect of water vapor fluctuations on n considerably exceeds that of temperature, so for simplicity we evaluate the temperature coefficient a for a dry atmosphere. The resulting expression is

$$n = 8.6 \times 10^{-7}\,(\theta - 7.8q), \tag{8}$$

for θ in kelvins and q in g kg^{-1}. Therefore, $\tilde{C}_n^2$ is

$$\tilde{C}_n^2 = 74.3 \times 10^{-14}\,(\tilde{C}_\theta^2 - 15.6\tilde{C}_{\theta q} + 60.8\tilde{C}_q^2), \tag{9}$$

where $\tilde{C}_\theta^2$ and $\tilde{C}_q^2$ are the local structure–function parameters of temperature and humidity, respectively, and $\tilde{C}_{\theta q}$ is the local joint structure–function parameter.

We calculate the local structure–function parameters as

$$\tilde{C}_\theta^2 = \frac{1.6}{\tilde{\epsilon}^{1/3}}\tilde{\chi}_{\theta^2}, \qquad \tilde{C}_q^2 = \frac{1.6}{\tilde{\epsilon}^{1/3}}\tilde{\chi}_{q^2},$$

$$\tilde{C}_{\theta q} = \frac{1.6}{\tilde{\epsilon}^{1/3}}\tilde{\chi}_{\theta q}. \tag{10}$$

The local dissipation rate of kinetic energy $\tilde{\epsilon}$ is given by

$$\tilde{\epsilon} = \left(0.19 + 0.74\frac{l}{\Delta s}\right)\frac{e^{3/2}}{l}, \tag{11}$$

where the effective scales Δs and l of the grid volume and the subgrid-scale turbulence, respectively, are

$$\Delta s = (1.5\Delta x \times 1.5\Delta y \times \Delta z)^{1/3},$$

$$l = \Delta s \qquad \text{if } \frac{\partial\theta^r}{\partial z} < 0$$

$$= 0.76\sqrt{\frac{e}{g/T_0\partial\theta^r/\partial z}} \quad \text{if } \frac{\partial\theta^r}{\partial z} > 0.$$

Here $\tilde{\chi}_{\theta^2}$, $\tilde{\chi}_q^2$, and $\tilde{\chi}_{\theta q}$ are the local rates of destruction of temperature variance, mixing ratio variance, and temperature–humidity covariance,

$$\tilde{\chi}_{\theta^2} = 2K\theta_{,i}^r\theta_{,i}^r, \qquad \tilde{\chi}_{q^2} = 2Kq_{,i}^r q_{,i}^r,$$

$$\tilde{\chi}_{\theta q} = 2K\theta_{,i}^r q_{,i}^r, \tag{12}$$

where q^r and θ^r are the resolvable-scale water vapor mixing ratio and temperture, respectively, and K is the subgrid-scale eddy diffusivity:

$$K = (1 + 2l/\Delta s)0.1l\sqrt{e}. \tag{13}$$

Moeng (1984) and Peltier and Wyngaard (1995) discuss those relations in detail.

The water vapor mixing ratio fields are generated by superposition of fields of top–down and bottom–up passive, conservative scalars calculated through large eddy simulation (Moeng and Wyngaard 1984). Denoting the fluctuating top–down and bottom–up scalar fields by c_t and c_b, the q field is taken as

$$q(\mathbf{x}, t) = c_1 c_t(\mathbf{x}, t) + c_2 c_b(\mathbf{x}, t). \tag{14}$$

The constants c_1 and c_2 are chosen such that the mixing ratio flux at the surface ($c_1\langle wc_b\rangle|_0$) and at the mixed-layer top ($c_2\langle wc_t\rangle|_{z_i}$) were 0.05 (gm of vapor) (kg of air)$^{-1}$ m s^{-1}. The resulting mixing ratio flux was nearly

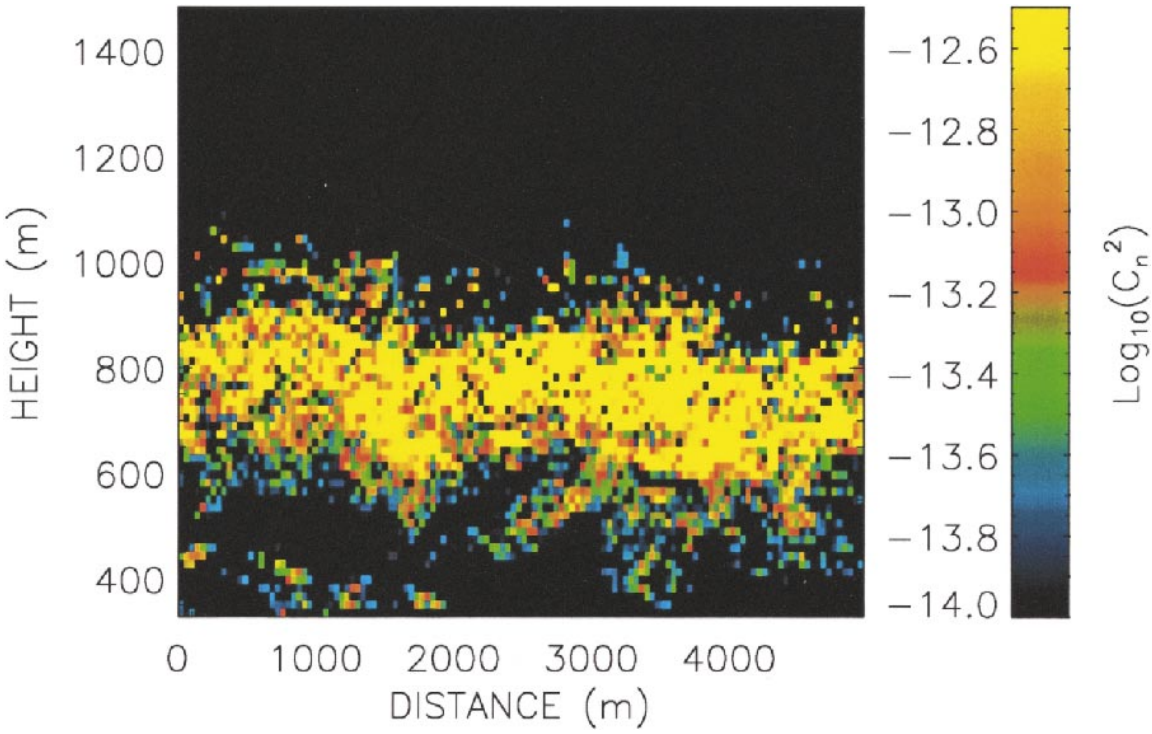

FIG. 8. A profile of the $\tilde{C}_n^2$ from a single vertical slice through the LES domain.

uniform throughout the mixed-layer depth. With (10) through (14), we calculate $\tilde{C}_n^2$ from (9).

As discussed by Peltier and Wyngaard (1995), LES does not model the local molecular destruction rates $\tilde{\epsilon}$ and $\tilde{\chi}$; it models the rates of inertial transfer of energy and scalar variance from resolvable scales to the subgrid scales. Because of the nature of the subgrid-scale variance budgets, these transfer rates can differ locally from the corresponding destruction rates, although their expected values are the same. We expect the extent to which the two quantities correlate increases with the scale of the local averaging volume, much as we expect the correlation of the TEP backscattered power ($\tilde{\eta}$) and $\tilde{C}_n^2$ to increase with increasing pixel size (appendix A). In the remainder of this paper, we examine the impact of those differences on LES $\tilde{C}_n^2$ by comparing the LES predictions to TEP measured values.

b. LES $\tilde{C}_n^2$ morphology

Typical instantaneous vertical structure of $\tilde{C}_n^2$ is shown in Fig. 4. A similar plot can be made for LES $\tilde{C}_n^2$ predictions by taking a vertical streamwise slice through the LES domain. Figure 8 shows such a plot, where the $\tilde{C}_n^2$ are plotted on a logarithmic scale similar to Fig. 4. The x axis of Fig. 8 is a distance of 5 km, which is roughly equivalent to the 50-min plots in Fig. 4. The TEP and LES vertical beam plots look quite similar in their contrast, especially in the high $\tilde{C}_n^2$ region surrounding the capping inversion layer. The LES predictions do not seem to contain, however, the structures that TEP shows in the lower boundary layer, especially in TEP segments N through P and in S and U.

Figures 5 and 6 show TEP measurements of 100-m-scale structures in $\tilde{C}_n^2$ and w. Previous work shows similar qualitative features from LES (Pollard et al. 1998). We can quantify the scales of the fluctuating LES $\tilde{C}_n^2$ as in the previous section through the calculation of the horizontal correlation distance, λ_η. We use (4) to estimate $\tilde{\eta}$ from the LES $\tilde{C}_n^2$, and calculate $\tilde{\eta}'$ by removing mean $\tilde{\eta}$ at each altitude throughout the LES domain. Then, as for TEP, λ_η is found from the $1/e$ point of the three-dimensional $R_{\eta\eta}$, computed from (6), where $\lambda_{\eta h}$ is the horizontal, streamwise correlation length.

Figure 9 shows the average $\lambda_{\eta h}$ from the LES $\tilde{C}_n^2$ set, with the LES results mapped into cones with the dimensions of the radar field of view. We have created 64 independent cones with the dimensions of the TEP field of view in the LES domain and computed the average correlation distance $\lambda_{\eta h}$ for three cases. In each case, $\lambda_{\eta h}$ is estimated along the mean wind direction. Figure 9 shows curves for the limits of the LES results mapped into the TEP cone dimensions, $\lambda_{\eta h}$ from the direct $R_{\eta\eta}$, and $\lambda_{\eta h}$ from the high-pass filtered $R_{\eta\eta}$, calculated with the mean removed in each field of view. The $\lambda_{\eta h}$ from the direct $R_{\eta\eta}$ curve is much closer to the cone limit than the radar curve at lower altitudes, but shows comparable structure near z_i. The high-pass $\lambda_{\eta h}$ curve, however, compares very well with the radar case, both in value and in slope. Thus, while the curves in

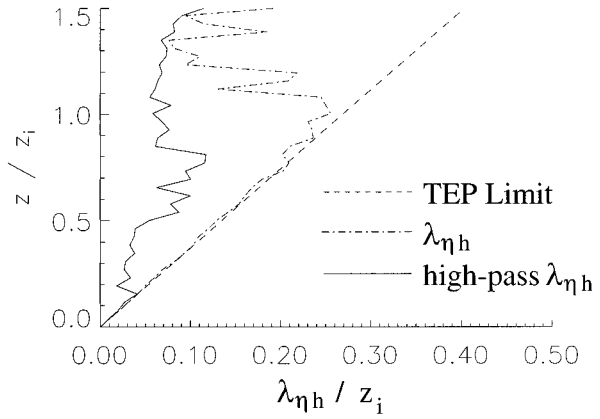

FIG. 9. Similar to Fig. 7 for LES data mapped into a volume equivalent to the TEP field of view. As in Fig. 7, the TEP limit represents the limits of the TEP field of view for a perfectly correlated scene, the total $\lambda_{\eta h}$ is calculated directly from the autocorrelation function for the fluctuating component of $\tilde{C}_n^2$, and the high-pass $\lambda_{\eta h}$ is calculated after removing the mean $\tilde{C}_n^2$ at each altitude in each TEP-like cone.

Figs. 7 and 9 show the limits of the TEP field of view in imaging $\tilde{C}_n^2$ structures, it is interesting to note that the behavior of the smaller structures represented by the $\lambda_{\eta h}$ of the high-pass filtered $\tilde{C}_n^2$ agrees well between the TEP measurements and LES predictions. The similarity of 100-m-scale $\tilde{C}_n^2$ features in (Pollard et al. 1998) also supports that conclusion.

6. Statistical comparisons

Although the TEP field of view is inadequate for capturing the largest $\tilde{C}_n^2$ features, we can construct larger effective volumes by examining TEP time series data and invoking Taylor's hypothesis. In this section, we examine the statistics of w and $\tilde{C}_n^2$ from volumes constructed from time series data. We also examine the measured horizontal correlation distance of $\tilde{C}_n^2$ structures.

One advantage of the TEP system over other vertically pointed systems in the analysis of time series data is the simultaneous measurement of pixels in the crosswind dimension. Figure 10 illustrates the time series data segments. The crosswind dimension includes multiple independent pixels and thus improves the time series statistics.

The TEP measurements within three-dimensional effective volumes are another opportunity for LES comparisons, and for each of the results presented below we also provide corresponding LES results. In each case we use four segments of TEP data to facilitate that comparison; with a mean wind speed near 2 m s^{-1}, four TEP data segments would form an equivalent distance of approximately 5 km, equivalent to the horizontal, streamwise dimension in the LES domain.

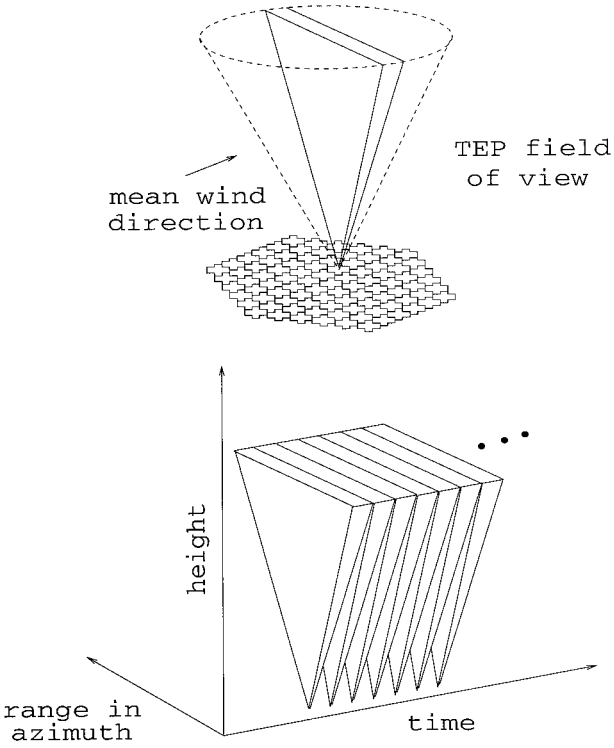

FIG. 10. The method used in forming three-dimensional volumes from crosswind slices through the TEP field of view. Crosswind slices are stacked in time, forming a three-dimensional dataset.

a. Vertical velocity statistics

The statistics of the vertical velocity w in the CBL are well studied, and provide a first-order comparison of LES with radar measurements. The second moment $\langle w^2 \rangle$ is calculated from the variance of w in each pixel over horizontal slices of constant normalized height. The mean of w at each height is very close to zero for both TEP and LES, as expected.

Figure 11 shows a comparison of the vertical velocity variances from TEP and LES. Here the radar data are taken from segments R to U, although all combinations of data segments show a similar behavior. The values shown are scaled by the respective convective velocity scales w_*, shown in Table 3. Below z_i the results compare well and are similar to those found in other LES studies (Moeng 1984; Mason 1989; Schmidt and Schumann 1989), and laboratory (Willis and Deardorff 1974; Deardorff and Willis 1985), and radar (Kropfli and Hildebrand 1980) measurements.

Above $1.0z_i$, however, the LES predictions diverge from the TEP measurements. The observation of increased vertical velocity variance above z_i is seen in other profiler data in (Angevine et al. 1994), and also in lidar data (Frehlich et al. 1998). One explanation for the difference between measurement and simulation is that there is atmospheric motion above $1.0z_i$ that is not well modeled by LES.

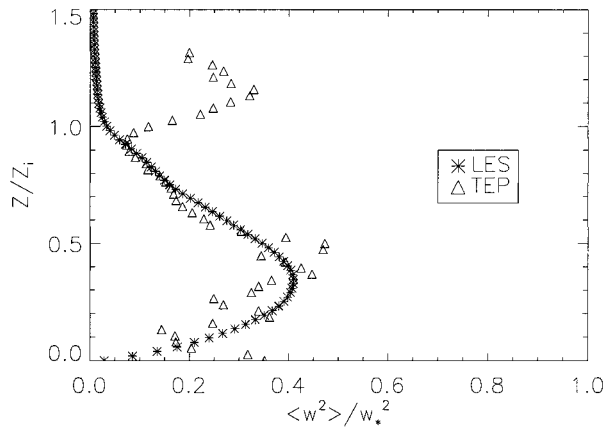

FIG. 11. A comparison of the variance of the vertical velocity, normalized by the convective velocity scale w_*. The TEP data segments used in this comparison are segments R–U.

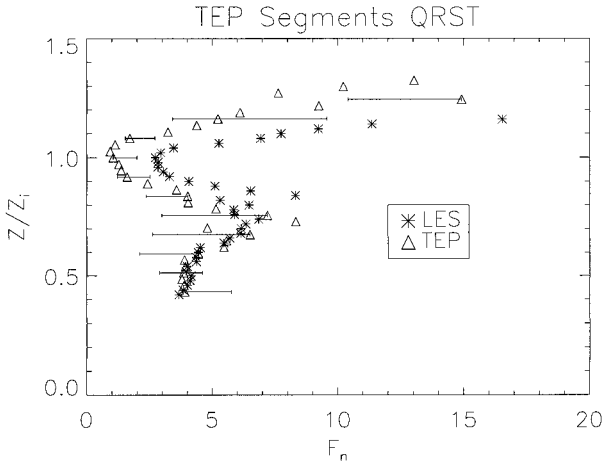

FIG. 12. A comparison of F_n, the variability index, for LES $\tilde{C}_n^2$ data over the full LES domain, and TEP time series $\tilde{C}_n^2$ data from segments QRST. The error bars note the extent of F_n from other sets of four TEP data segments.

b. Statistics of $\tilde{C}_n^2$

Peltier and Wyngaard (1995) present the results of their LES structure–function parameter calculations in terms of a ''variability index,'' or normalized variance F_n:

$$F_n = \frac{\text{variance of } \tilde{C}_n^2}{\text{squared mean of } \tilde{C}_n^2}. \tag{15}$$

Here F_n is calculated as the variance of $\tilde{C}_n^2$ over slices of constant altitude, similar to the $\langle w^2 \rangle$ calculation in the previous section. At each height, the variance is normalized by the squared mean of $\tilde{C}_n^2$ at that altitude.

In analyzing TEP F_n measurements, two factors need be considered. First, it is important to quantify the effects of fading on a variance calculated from the radar data. Each radar power estimate is subject to Rayleigh fading statistics that limit the accuracy of that estimate; a single estimate has a normalized variance of unity (Ulaby et al. 1982, p. 480). The variance due to fading is reduced by a factor of N_i by averaging N_i independent samples. For each estimate, we average two 64-point FFTs, each spanning 0.64 s. The tails of the measured spectrum typically fill more than 8 FFT bins, implying that each spectrum represents roughly 8 independent samples. Those 8 samples along with the factor of 2 from incoherently averaging two spectra, reduce the normalized error in the power estimate due to fading to 6% of the estimated value (± 0.27 dB). That error is small compared to the variance obtained from TEP data, presented below.

Second, the pixel efficiency should be considered in TEP $\tilde{C}_n^2$ estimates. We define the pixel efficiency ϵ as the ratio of the power received from within a single pixel to the total power received. Here, the pixels are defined by the 6-dB contour of the radar beam. With that definition,

$$P_m = \epsilon P_a + (1 - \epsilon) P_s, \tag{16}$$

where P_m is the measured return power in each pixel, P_a is the actual power that would be measured by the sensor having a perfect pixel efficiency, and P_s is the power received from pixels outside of the main beam. As discussed in Mead et al. (1998), the TEP antenna pattern, or any real antenna pattern, has a ϵ less than 1. With the TEP receiver array, however, phase errors between the many elements reduce the pixel efficiency to values near 70% (Mead et al. 1998).

For statistical comparisons, we define F_a as the normalized variance of the actual power return from each pixel:

$$F_a = \frac{\sigma_a^2}{\langle P_a \rangle^2} = \frac{\langle P_a^2 \rangle - \langle P_a \rangle^2}{\langle P_a \rangle^2}. \tag{17}$$

It is shown in appendix B that the actual normalized variance F_a, is

$$F_a \approx \frac{1}{\epsilon^2} F_m \approx 2F_m, \tag{18}$$

for a beam efficiency of 70%, where F_m is defined for P_m similarly to F_a in (17). Equation (18) corrects each of the measured values presented in this paper.

The results of the TEP F_n calculations are presented in Fig. 12, where segments Q through T are shown by the triangles. Here F_n is only calculated above $0.4z_i$, as results below that altitude are highly intermittent due to occasional clutter sources. The F_n values seem to increase with increasing height up to approximately $0.75z_i$, near the edge of the high $\tilde{C}_n^2$ region surrounding z_i. Above $0.75z_i$ F_n begins to decrease, reaching a minimum at z_i. The increase above z_i is due to the decreasing denominator in (15) as well as the changing thickness of the high $\tilde{C}_n^2$ region.

Segments Q through T are shown because they agree quite closely to the LES F_n, the stars in Fig. 12. The

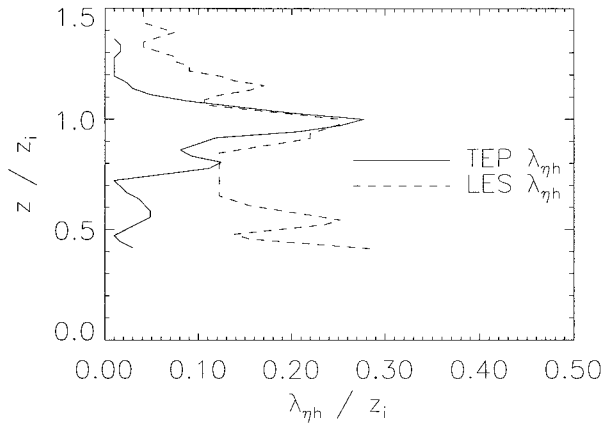

FIG. 13. The correlation distance $\lambda_{\eta h}$ for $\tilde{C}_n^2$ structures in the full LES domain and from TEP data segments R–U. The TEP data is actually a correlation lag time that is multiplied by a 2 m s^{-1} mean wind speed to produce a correlation distance.

shape of the two curves agrees quite well, while the differences in value near $1.0z_i$ could be due to the F_n correction, as is discussed in the appendix. With other TEP datasets, however, the LES F_n agrees less well. The error bars in Fig. 12 show the minimum and maximum F_n from other combinations of four adjacent TEP data segments. The general shape presented by the error bars, however, seems similar to segments Q through T.

c. $\tilde{C}_n^2$ autocorrelations

As in section 4.2, we can calculate the temporal (TEP) or spatial (LES) autocorrelation functions to examine the scales of $\tilde{C}_n^2$ structures. We again calculate the autocorrelation function $R_{\eta\eta}$ from the inverse Fourier transform of the three-dimensional spectral density of $\tilde{\eta}'$ at each altitude and determine $\lambda_{\eta h}$, the horizontal correlation distance. The TEP values are presented as a normalized distance by multiplying the observed correlation lag time in the temporal dimension by the mean wind. Both TEP and LES calculations are in the streamwise direction.

Figure 13 shows the TEP and LES $\lambda_{\eta h}$ vertical profiles. The radar data are taken from segments R to U, but all combinations of four adjacent segments show very similar behavior. As in the previous section, only results above $0.4z_i$ are shown. The TEP curve shows a small $\lambda_{\eta h}$ with a fairly constant slope up through $0.75z_i$. Above $0.75z_i$ the TEP $\lambda_{\eta h}$ curve behaves as expected, with the largest correlation distance occurring near z_i, the area of largest $\tilde{C}_n^2$ structure.

Near z_i, the LES $\lambda_{\eta h}$ agrees well with the measurements. However, the LES values in the mid-boundary layer are much larger than the TEP measured $\lambda_{\eta h}$. One explanation for that difference is due to the lack of narrow plumes of $\tilde{C}_n^2$ in the LES results. The TEP vertical profiles of $\tilde{C}_y^2$ shown in Fig. 4 show several narrow plumes of high $\tilde{C}_n^2$ that do not appear in the LES $\tilde{C}_n^2$ predictions shown in Fig. 8. Those plumes account for the small TEP $\lambda_{\eta h}$ measurements in the mid-boundary layer. LES, on the other hand, may predict coherent structures with small values of $\tilde{C}_n^2$ that are not easily measured by radars due to limitations in sensitivity. The differences here will be a topic of future research.

7. Summary

This paper shows a unique dataset from the CBL obtained with the TEP radar system. We present qualitative and quantitative measurements of the CBL and examine $\tilde{C}_n^2$ and w statistics through time series measurements.

Measured vertical profiles of $\tilde{C}_n^2$ show a bright band near the capping inversion layer, z_i. The vertical profiles also show intermittent plumes of enhanced $\tilde{C}_n^2$ in the mid-boundary layer. In the horizontal TEP images, we find 100-m-scale coherent structures of enhanced $\tilde{C}_n^2$ that correspond to converging horizontal winds and coherent downdrafts in w. The presented feature has a vertical extent of $0.05z_i$.

The three-dimensional autocorrelation function is calculated within the TEP field of view and we have presented the vertical and streamwise correlation distances, λ_η, for the fluctuating component of $\tilde{C}_n^2$. In the streamwise direction, TEP measures the full scales of structures in the lower boundary layer, but does not capture the full scales of structures near z_i.

We compare LES $\tilde{C}_n^2$ predictions to the radar measurements and find a similar vertical profile, although missing the plumes of high $\tilde{C}_n^2$ in the lower boundary layer that occur in the measured data. The streamwise, horizontal λ_η is calculated from the LES $\tilde{C}_n^2$ set mapped into cones of TEP-like dimensions and the LES results agree well with the measured data.

To study larger-scale features, we construct effective volumes from the measured time series data. Those volumes differ from those formed with traditional, vertically profiling instruments, as the TEP volumes add a crosswind dimension improving the statistics of our estimates. We compare the measured variability of $\tilde{C}_n^2$ and w in those volumes to LES.

TEP and LES curves of w variance reproduce well-known results in the boundary layer. Above z_i, however, the measured and simulated values diverge, a result seen in other recently published remotely sensed data. That divergence may well be due to atmospheric motions above the capping inversion layer that are not well modeled by LES.

The measurements of $\tilde{C}_n^2$ variance show a vertical profile that is consistent with the qualitative results. The LES $\tilde{C}_n^2$ variance agrees well with the some, but not all of the measured data. Some of the differences between measured and simulated values may be due to the effects of pixel efficiency, as discussed in appendix B.

We have also compared correlation distances from TEP time series data with LES. The two agree well in

the region surrounding the capping inversion layer, but the radar measures a much lower correlation distance below $0.75z_i$ than predicted by LES. That difference is perhaps due to the lack of narrow plumes in the LES $\tilde{C}_n^2$ predictions and will be a subject of further study.

In summary, we have found many similarities in $\tilde{C}_n^2$ from TEP measurements and LES predictions, suggesting that LES predictions are quite good, not only in their statistical behavior, but also in their local, instantaneous behavior. The differences we have found occur in the mid- to lower boundary layer and require further study. The results here suggest, however, that LES may well become a useful tool in the simulation of electromagnetic propagation in the ABL.

Finally, this study introduces some of the unique capabilities of the TEP instrument. The ability to image structures throughout the boundary layer with a high time resolution is applied here to LES CBL comparisons of $\tilde{C}_n^2$ and velocity vectors, but in the future may be applied to many other problems of interest.

Acknowledgments. This work was supported by the U. S. Army Research Office under Grant DAAL03-92-G-0110 at UMass and Grant DAAL03-92-G-0117 at PSU. The authors would like to thank Chenning Tong for collecting and analyzing the anemometer data, Dick Thompson for his extensive help at the Rock Springs site, Minfei Leng for his assistance in the TEP deployment at Rock Springs, and Geoff Hopcraft for his assistance in the TEP system development. The authors also would like to thank Jim Mead and Keith Wilson for helpful discussions, and the three reviewers for their helpful comments.

APPENDIX A

A Discussion of $\tilde{C}_n^2$ and $\tilde{\eta}$

The roots of (1) and (2) lie in the hypotheses of Kolmogorov (1941) concerning the structure of turbulence in the inertial subrange of wavenumbers, that is, turbulence at spatial scales small compared to those of the energy-containing range, but large compared to those of the dissipative range. The extent of this inertial subrange is proportional to $R_t^{3/4}$ (Tennekes and Lumley 1972), where R_t is a Reynolds number of the energy-containing turbulence. Here R_t is typically so large in the atmospheric boundary layer that the inertial subrange there is at least a decade wide, and often wider.

As discussed in section 2, also central to (1) and (2) is the notion of the ensemble average. Equations (1) and (2) are purely statistical relations that emerge only after sufficient averaging. We typically use a time average in place of an ensemble average and assume ergodicity (Tennekes and Lumley 1972).

Short-term averages of backscattered power and of squared, two-point differences in refractive index vary considerably in time and in space. Their expected values can, of course, depend on time and on position in a flow, but due to the smoothing effects of the ensemble averaging operator any temporal or spatial variations in expected values are also smooth; they vary on the timescale of mean flow evolution and on the spatial scale of mean flow structure. The faster, smaller-scale variations in backscattered power and in refractive-index structure should not be interpreted as variations in η and C_n^2.

The fluctuating refractive index n depends on fluctuating temperature and fluctuating water vapor mixing ratio q (section 5). For simplicity in this discussion let us take the refractive-index fluctuations to be dominated by the water vapor contribution, so $n = cq$ with c a constant (section 5). It follows that $C_n^2 = c^2 C_q^2$. By the Kolmogorov (1941) hypothesis

$$C_q^2 = 1.6\epsilon^{-1/3}\chi_q, \tag{A1}$$

where ϵ is the dissipation rate of turbulent kinetic energy per unit mass and χ_q is the molecular destruction rate of $\langle q^2 \rangle$. The C_q^2, ϵ, and χ_q are ensemble-mean quantities.

During the years following Kolmogorov's (1941) hypotheses, turbulence researchers discovered that the small-scale properties of turbulence in large R_t flows are quite nonuniformly distributed in space at any given time and quite intermittent in time at a given point in space. Thus, short time averages of statistics of finescale properties, such as the dissipation rate of turbulence energy and molecular destruction rate of squared water vapor fluctuations, can have large fluctuation levels. Kolmogorov (1962) and Obukhov (1962) introduced the notion of finescale properties averaged over a local volume of space of characteristic dimension r, and reinterpreted Kolmogorov's original (1941) hypotheses in terms of these *local* variables, as we will call them.

In this spirit Peltier and Wyngaard (1995) define *local* structure–function parameters. The local version of (A1) for water vapor is

$$\tilde{C}_q^2 = 1.6\tilde{\epsilon}^{-1/3}\tilde{\chi}_q, \tag{A2}$$

the tilde denoting the Kolmogorov–Obukhov volume average. Here $\tilde{C}_q^2$ is a random variable. Its expected value is the traditional structure–function parameter:

$$\langle \tilde{C}_q^2 \rangle = C_q^2. \tag{A3}$$

Similarly, we can define a local backscattered power coefficient $\tilde{\eta}$, a random variable whose expected value is η.

By the revised Kolmogorov–Obukhov hypotheses the counterpart to (1) but for local variables is

$$\langle \tilde{\eta} \,|\, \tilde{C}_n^2 \rangle = 0.38\tilde{C}_n^2\lambda^{-1/3}, \tag{A4}$$

$\langle \tilde{\eta} \,|\, \tilde{C}_n^2 \rangle$ being the expected value of $\tilde{\eta}$, the instantaneous but volume-averaged backscattered power coefficient, for realizations in which the local structure–function parameter has the value $\tilde{C}_n^2$. The unaveraged, unconditional result of (4), $\tilde{\eta} = 0.38\tilde{C}_n^2\lambda^{-1/3}$, does not directly follow, however. Thus, the Kolmogorov–Obukhov hy-

potheses do not directly imply that the local backscattered power coefficient ''tracks'' (is perfectly correlated with) the local structure function parameter.

Wilson et al. (1996) have shown how the Kolmogorov–Obukhov hypotheses can be applied in terms of probability densities. The conditionally averaged backscattered power coefficient $\langle\tilde{\eta}|\,\tilde{C}_n^2\rangle$ is

$$\langle\tilde{\eta}|\,\tilde{C}_n^2\rangle = \int_0^\infty \beta_1(\tilde{\eta}|\,\tilde{C}_n^2)\tilde{\eta}\,d\tilde{\eta}, \tag{A5}$$

where $\beta_1(\tilde{\eta}|\,\tilde{C}_n^2)$ is a conditional probability density; the probability density of $\tilde{\eta}$ given that the local structure–function parameter has the value $\tilde{C}_n^2$. We can also write

$$\eta = \int_0^\infty \beta_2(\tilde{\eta})\tilde{\eta}\,d\tilde{\eta}. \tag{A6}$$

The unconditional probability density $\beta_2(\tilde{\eta})$ is an integral of the conditional density,

$$\beta_2(\tilde{\eta}) = \int_0^\infty \beta_1(\tilde{\eta}|\,\tilde{C}_n^2)\beta_3(\tilde{C}_n^2)\,d\tilde{C}_n^2. \tag{A7}$$

If the conditional density has the property

$$\beta_1(\tilde{\eta}|\,\tilde{C}_n^2) = \delta(\tilde{\eta} - 0.38\tilde{C}_n^2\lambda^{-1/3}), \tag{A8}$$

then the probability densities of $\tilde{\eta}$ and $\tilde{C}_n^2$ are identical and the local backscattered power coefficient $\tilde{\eta}$ tracks the local structure–function parameter $\tilde{C}_n^2$ perfectly.

We do not expect, in general, that $\tilde{\eta}$ and $\tilde{C}_n^2$ track perfectly, or, equivalently, that (A8) holds. Given the Kolmogorov–Obukhov arguments we expect the finite size of the averaging volume to cause decorrelation of $\tilde{\eta}$ and $\tilde{C}_n^2$. We also expect that as the radar sampling (averaging) time approaches the timescales of variability, $\tilde{\eta}$ and $\tilde{C}_n^2$ decorrelate (D. K. Wilson 1998, personal communication). Thus we expect that as sampling times and pixel sizes shrink, (A8) and thus (4) become less valid. We do not know, however, at what time and spatial scales we may still assume the validity of (4). The comparisons of $\tilde{C}_n^2$ in this paper suggest that, at least for the TEP case, (4) is still a good approximation.

APPENDIX B

Pixel Efficiency

The definition of the pixel efficiency ϵ is used to form (16) above,

$$P_m = \epsilon P_a + (1 - \epsilon)P_s, \tag{B1}$$

where P_m is the measured return power in each pixel, P_a is the actual power that would be measured by a sensor with a perfect pixel efficiency, and P_s is the power received from outside of the main beam. Using the variability index of (15) for $\sigma_a^2 = \langle P_a^2\rangle - \langle P_a\rangle^2$ yields

$$F_a = \frac{\sigma_a^2}{\langle P_a\rangle^2} = \frac{\sigma_m^2 + (1-\varepsilon)^2\sigma_s^2 - 2(1-\varepsilon)[\langle P_m P_s\rangle - \langle P_m\rangle\langle P_s\rangle]}{\langle P_m\rangle^2 - 2(1-\varepsilon)\langle P_m\rangle\langle P_s\rangle + (1-\varepsilon)^2\langle P_s\rangle^2}. \tag{B2}$$

We can assume that

$$\langle P_m\rangle = \langle P_s\rangle = \langle P_a\rangle \tag{B3}$$

if the endfire antenna pattern is sufficiently below the power in the main beam, a good assumption for the TEP system. Equation (B3) suggests that the extra contributions from outside the main beam are due to near-in sidelobes and are from atmospheric targets. With that assumption,

$$F_a = \frac{\sigma_m^2 + (1-\varepsilon)^2\sigma_s^2 - 2(1-\varepsilon)[\langle P_m P_s - \langle P_m\rangle^2]}{\varepsilon^2\langle P_m\rangle^2}. \tag{B4}$$

Examining the third term of (30) shows that

$$\frac{2(1-\varepsilon)[\langle P_m P_s\rangle - \langle P_m\rangle^2]}{\varepsilon^2\langle P_m\rangle\langle P_m\rangle} = \frac{2(1-\varepsilon)}{\varepsilon^2}\left[\frac{\langle P_m P_s\rangle}{\langle P_m\rangle\langle P_s\rangle} - 1\right]. \tag{B5}$$

The quantity $\langle P_m P_s\rangle/\langle P_m\rangle\langle P_s\rangle$ is unity if P_m and P_s are independent, and for simplicity that assumption is used, implying that the third term of (B4) can be ignored.

Dropping the third term of (B4) yields

$$F_a = \frac{\sigma_m^2 + (1-\varepsilon)^2\sigma_s^2}{\varepsilon^2\langle P_m\rangle^2}, \tag{B6}$$

which is equivalent to

$$F_a = \frac{1}{\varepsilon^2}F_m - \frac{(1-\varepsilon)^2}{\varepsilon^2}F_s. \tag{B7}$$

A typical pixel efficiency is approximately 70%. In (B7) that makes the F_s term 0.18 times the F_m term, implying that even if $F_s \approx F_m$, the error in assuming

$$F_a \approx \frac{1}{\varepsilon^2}F_m \tag{B8}$$

is less than 10%. Of course, since F_s is sampled from a much broader scene it should be less than F_m, and the relationship in (B8) should be a good approximation, albeit perhaps somewhat low because the term examined in (B5) is ignored. That term, ignored by assuming that P_m and P_s are independent, may explain the slightly lower values of the TEP F_n when compared to the LES values.

REFERENCES

Angevine, W. M., R. J. Doviak, and Z. Sorbjan, 1994: Remote sensing of vertical velocity variance and surface heat flux in a convective boundary layer. *J. Appl. Meteor.*, **33,** 977–983.

Deardorff, J. W., 1972: Numerical investigations of neutral and unstable planetary boundary layers. *J. Atmos. Sci.,* **29,** 91–115.
——, and G. E. Willis, 1985: Further results from a laboratory model of the convective boundary layer. *Bound.-Layer Meteor.,* **32,** 205–236.
Doviak, R. J., and M. Berger, 1980: Turbulence and waves in the optically clear planetary boundary layer resolved by dual-Doppler radars. *Radio Sci.,* **15,** 297–317.
Eaton, F. D., S. A. McLaughlin, and J. R. Hines, 1995: A new frequency-modulated continuous wave radar for studying planetary boundary layer morphology. *Radio Sci.,* **30,** 75–88.
Ecklund, W. L., D. A. Carter, and B. B. Balsley, 1988: A UHF wind profiler for the boundary layer: Brief description and initial results. *J. Atmos. Oceanic Technol.,* **5,** 432–441.
——, P. E. Johnston, W. L. Clark, J. M. Warnock, T. E. VanZandt, and K. S. Gage, 1996: Scattering from clear air, precipitation, and biological targets: Multiple frequency profiler studies. *Proc. Seventh MST Radar Workshop,* Hilton Head Island, SC, Solar–Terresterial Energy Program, 32–35.
——, C. R. Williams, P. E. Johnston, and K. S. Gage, 1999: A 3-GHz profiler for precipitating cloud studies. *J. Atmos. Oceanic Technol.,* **16,** 309–322.
Frehlich, R., S. M. Hannon, and S. W. Henderson, 1998: Coherent Doppler lidar measurements of wind field statistics. *Bound.-Layer Meteor.,* **86,** 233–256.
Gossard, E. E., 1990: Radar research on the atmospheric boundary layer. *Radar in Meteorology,* D. Atlas, Ed., Amer. Meteor. Soc., 477–527.
——, R. B. Chadwick, W. D. Neff, and K. P. Moran, 1982: The use of ground-based Doppler radars to measure gradients, fluxes, and structure parameters in elevated layers. *J. Appl. Meteor.,* **21,** 211–226.
Hardy, K. R., and H. Ottersten, 1969: Radar investigations of convective patterns in the clear atmosphere. *J. Atmos. Sci.,* **26,** 666–672.
Khanna, S., and J. C. Wyngaard, 1997: Local refractive index structure-function parameter and its application to wave propagation. *Proc. 1996 Battlespace Atmospherics Conf.,* San Diego, CA, NRaD Tech Doc. 2938, 433–440.
——, and J. G. Brasseur, 1998: Three dimensional buoyancy- and shear-induced local structure of the atmospheric boundary layer. *J. Atmos. Sci.,* **55,** 710–743.
Kolmogorov, A. N., 1941: The local structure of turbulence in incompressible viscous fluid for very large Reynolds numbers. *C. R. Seances Acad. Sci.,* **30,** 301–305.
——, 1962: A refinement of previous hypotheses concerning the local structure of turbulence in a viscous incompressible fluid at high Reynolds number. *J. Fluid Mech.,* **13,** 82–85.
Konrad, T. G., 1970: The dynamics of the convective process in clear air as seen by radar. *J. Atmos. Sci.,* **27,** 1138–1147.
Kropfli, R. A., and P. H. Hildebrand, 1980: Doppler radar measurements in the planetary boundary layer during PHOENIX. Preprints, *19th Conf. on Radar Meteorology,* Miami Beach, FL, Amer. Meteor. Soc., 637–644.
Lenschow, D. H., and B. B. Stankov, 1986: Length scales in the convective boundary layer. *J. Atmos. Sci.,* **43,** 1198–1209.
Mason, P. J., 1989: Large-eddy simulation of the convective atmospheric boundary layer. *J. Atmos. Sci.,* **46,** 1492–1516.
Mead, J. B., G. Hopcraft, S. J. Frasier, B. D. Pollard, C. D. Cherry, D. H. Schaubert, and R. E. McIntosh, 1998: A volume-imaging radar wind profiler for atmopsheric boundary-layer turbulence studies. *J. Atmos. Oceanic Technol.,* **15,** 849–859.
Moeng, C. H., 1984: A large eddy simulation model for the study of planetary boundary-layer turbulence: *J. Atmos. Sci.,* **41,** 2052–2062.
——, and J. C. Wyngaard, 1984: Statistics of conservative scalars in the convective boundary layer. *J. Atmos. Sci.,* **41,** 3161–3169.
Obukhov, A. M., 1962: Some specific features of atmospheric turbulence. *J. Fluid Mech.,* **13,** 77–81.
Ottersten, H., 1969: Atmospheric structure and radar backscattering in clear air. *Radio Sci.,* **4,** 1179–1193.
Peltier, L. J., and J. C. Wyngaard, 1995: Structure-function parameters in the convective boundary layer from large eddy simulation. *J. Atmos. Sci.,* **52,** 3641–3660.
Pollard, B. D., S. Khanna, S. J. Frazier, J. C. Wyngaard, D. W. Thomson, and R. E. McIntosh, 1998: Convective boundary layer features from a volume-imaging radar and large-eddy simulations. *Proc. 1997 Battlespace Atmospherics Conf.,* San Diego, CA, NRaD Tech Doc. 2989, 349–357.
Richter, J. H., 1969: High resolution tropospheric radar sounding. *Radio Sci.,* **4,** 1261–1268.
Schmidt, H., and U. Schumann, 1989: Coherent structure of the convective boundary layer derived from large-eddy simulations. *J. Fluid Mech.,* **200,** 511–562.
Stull, R. B., 1988: *An Introduction to Boundary Layer Meteorology.* Kluwer Academic Publishers, 666 pp.
Tatarskii, V. I., 1971: *The Effects of the Turbulent Atmosphere on Wave Propagation.* Kefer Press, 472 pp. [NTIS TT 68-50464.]
Tennekes, H., and J. L. Lumley, 1972: *A First Course in Turbulence.* The MIT Press, 300 pp.
Ulaby, F. T., R. K. Moore, and A. K. Fung, 1982: *Microwave Remote Sensing (Active and Passive).* Vol. 2. Artech House, 2162 pp.
Wesely, M. L., 1976: The combined effect of temperature and humidity fluctuations on refractive index. *J. Appl. Meteor.,* **15,** 43–49.
White, A. B., C. W. Fairall, and D. W. Thomson, 1991: Radar observations of humidity variability in and above the marine atmospheric boundary layer. *J. Atmos. Oceanic Technol.,* **8,** 639–658.
Willis, G. E., and J. W. Deardorff, 1974: A laboratory model of the unstable planetary boundary layer. *J. Atmos. Sci.,* **31,** 1297–1307.
Wilson, D. K., J. C. Wyngaard, and D. I. Havelock, 1996: The effect of turbulent intermittency on scattering into an acoustic shadow zone. *J. Acoust. Soc. Amer.,* **99,** 3393–3400.
Wilson, J. W., T. M. Weckwerth, J. Vivekanandan, R. M. Wakimoto, and R. W. Russell, 1994: Boundary layer clear-air radar echoes: Origin of echoes and accuracy of derived winds. *J. Atmos. Oceanic Technol.,* **11,** 1184–1206.
Wyngaard, J. C., and M. A. LeMone, 1980: Behavior of the refractive index structure parameter in the entraining convective boundary layer. *J. Atmos. Sci.,* **37,** 1573–1585.